Lawrence Berkeley National Laboratory

Title

Imaging Atomic-Scale Clustering in III—V Semiconductor Alloys

Permalink

https://escholarship.org/uc/item/8xp3v2q2

Journal

ACS Nano, 11(3)

ISSN

1936-0851

Authors

Hirst, Louise C
Kotulak, Nicole A
Tomasulo, Stephanie
et al.

Publication Date

2017-03-28

DOI

10.1021/acsnano.6b07732

Peer reviewed

Imaging atomic scale clustering in III-V semiconductor alloys

Louise C. Hirst,*,† Nicole A. Kotulak,† Stephanie Tomasulo,† Josh Abell,† María González,‡ Michael K. Yakes,† Jerry R. Meyer,† Robert J. Walters,† Chengyu Song,¶ Petra Specht,§ Peter Ercius,¶ and Christian Kisielowski¶

†*U. S. Naval Research Laboratory, 4555 Overlook Ave. SW, 20375, USA*
‡*Sotera Defense Solutions, Inc., Annapolis Junction, Maryland 20701-1067, USA*
¶*The Molecular Foundry, Lawrence Berkeley National Laboratory, Berkeley, CA, USA*
§*University of California, Berkeley 94720, USA*

E-mail: louise.hirst@nrl.navy.mil

Abstract

Quaternary alloys are essential for the development of novel, high performance opto-electronic devices. However, immiscibility of the constituent elements can make these materials vulnerable to phase segregation, which degrades the optical and electrical properties of the solid. High efficiency III-V photovoltaic cells are particularly sensitive to this degradation. InAlAsSb lattice matched to InP is a promising candidate material for high bandgap subcells of a multi-junction photovoltaic device. However, previous studies of this material have identified characteristic signatures of compositional variation, including anomalous low energy photoluminescence. In this work, atomic scale clustering is observed in InAlAsSb via quantitative scanning transmission electron microscopy. Image quantification of atomic column intensity ratios enables comparison

1

with simulated images, confirming the presence of non-random compositional variation in this multi-species alloy.

Keywords

HAADF, image quantification, III-V alloys, clustering

Introduction

As optoelectronic devices evolve, novel III-V quaternary alloys are increasingly employed to engineer the combination of specific bandgaps and band alignments necessary to achieve new functionality and high performance. While lattice mismatch techniques such as metamorphic growth and mechanical stacking can provide access to a wider range of materials, fully lattice matched epitaxial growth on standard substrates remains the best method for obtaining the highest quality III-V materials.

Compounds lattice matched to InP present a particular opportunity for high efficiency multi-junction photovoltaics because of the wide range of direct bandgaps available. The quaternary alloys InGaAlAs and InGaAsP have direct bandgaps, lattice matched to InP, spanning the energy ranges 0.74 - 1.45 eV and 0.74 - 1.35 eV, respectively. These alloys have been extensively studied[1–5] and utilized for photovoltaic applications. A promising candidate material for achieving even higher bandgaps lattice matched to InP is the quaternary alloy InAlAsSb. This material has received much less experimental attention, and hence there is still some uncertainty in the exact bandgap range achievable. However, direct bandgaps spanning the range 1.45 - 1.81 eV have been predicted using interpolation methods.[6] Simulations show that multi-junction photovoltaic devices, with the potential to reach 50% conversion efficiency, could be developed using the extensive design space of quaternary alloys lattice matched to InP.[7–10] In practice, quaternary alloy growth can be challenging because the immiscibility of certain compositions can lead to phase segregation within the solid, which

degrades the material's optical and electronic properties. Phase segregation has previously been indicated in InAlAsSb by photoluminescence (PL) spectroscopy, including anomalously low PL emission with an S-shaped temperature dependence.[11] Similar behaviour has been widely described in other III-V alloys, most notably InGaN,[12] and the characteristic luminescence signatures of phase segregation are well documented. The task, however, of imaging inhomogeneity or clusters in these materials via electron microscopy for an unambiguous description of the atomic arrangement within the lattice has historically been difficult.[13] The main challenges for imaging III-V phase segregation by electron microscopy are: 1) in many of these materials clustering is likely to occur on an atomic scale, close to the resolution limit of modern equipment; 2) ultra-thin samples are necessary to observe compositional variation on this length scale, thus specially formulated low damage sample preparation techniques are required; 3) precise thickness measurements of these ultra-thin samples are necessary to discern clustering from random statistical variations in the alloy; 4) comparison with image simulations for quantification and compositional analysis becomes increasingly complex, and has greater uncertainty in an alloy with four atomic species.

While in the case of InGaN some authors have presented evidence of non-random compositional fluctuations by high resolution transmission electron microscopy,[14,15] the question of sample damage occuring during the imaging process is a critical concern and has been the subject of much discussion. It has been proposed that electron beam exposure can induce atomic re-arrangement in the sample, artificaly creating indium clusters[16–18] that are not present in the material as grown. As such, the effect of electron dose must be considered to eliminate this possiblity.[19,20] In recent months, atom probe tomography (APT) has been successfully applied to this problem, with various authors identifying clustering in InGaN[21] and InAlAsSb.[22,23] While this chemical analysis technique provides new insights regarding the particular species that are clustering, and even associated length scales, it is not a direct substitute for electron micrscopy as it does not provide structural information about the atomic lattice.

In this paper, we individually address the challenges outlined above to confirm atomic scale clustering in InAlAsSb via high-angle annular dark-field (HAADF) scanning transmission electron microscopy (STEM) imaging. Quaternary alloy compositions can be expressed as a fraction of two end point ternaries, $In_{0.52}Al_{0.48}As$ and $AlAs_{0.56}Sb_{0.44}$ in the present case. In this study clustering was experimentally analyzed for $(InAlAs)_x(AlAsSb)_{1-x}$ with composition x = 0.8, which is equivalent to composition $In_{0.42}Al_{0.58}As_{0.91}Sb_{0.09}$. Previous luminescence studies have shown degraded optical properties for InAlAsSb with this alloy composition.[24]

Evaluating thickness to distinguish between non-random clustering and random alloy variation

STEM images show a 2-dimensional projection of a 3-dimensional foil, hence sample thickness critically affects features in the image. Hernández-Saz et al.[22] recently reported the observation of In-rich and Sb-rich domains using radial distribution function analysis of APT data, with a length scale of ~2 nm. Clustering on this short length scale will only be observable by STEM in ultra-thin foils, however, on this length scale random variations in the alloy will also be observable. This complication is exacerbated in a quaternary alloy where the number of possible configurations increases substantially. The extent of the random variation observable in a STEM image is critically determined by foil thickness. It is therefore essential to evaluate the film thickness at the position where the image is acquired, in order to distinguish random variation from statistically non-random clustering.

Measurements performed using position averaged convergent beam electron diffraction (PACBED)

A PACBED pattern is produced by incoherently averaging convergent beam electron diffraction (CBED) patterns while scanning the probe across the imaging area. The resulting pattern with many overlapping disks is highly sensitive to sample thickness. Comparison with image simulation allows for an accurate determination of the sample thickness. This technique developed by LeBeau et al.[25] in recent years for quantitative STEM analysis is particularly well suited to measuring ultra-thin films where more traditional methods such as electron energy loss spectroscopy (EELS) are less reliable.[25] For each HAADF-STEM image, a corresponding PACBED pattern was acquired, scanning the probe across the same area to give a thickness evaluation for each acquisition. Image simulations were performed using the Dr. Probe multi-slice simulation package.[26] A random supercell structure with x-y dimensions 10 x 10 nm was simulated. The probe position was scanned over 16 unit cells of the simulated structure sampling 140 different positions. For each probe position, wavefunctions were calculated for each atomic layer throughout the supercell. A Fourier transform was performed on the wavefunction data, and the square moduli of the output were averaged to produce the simulated PACBED patterns. Input Debey-Waller factors were interpolated from literature values. See the supporting material for further details. Experimental PACBED patterns, taken from the same $(InAlAs)_{0.8}(AlAsSb)_{0.2}$ foil at different locations, are shown in Figure 1. The sample milling produces a shallow wedge shape, and hence as the imaging location moves further from the foil edge the sample becomes thicker. This is observed as an increase in PACBED pattern complexity. A line scan across the center of the pattern was performed in each case, and the best fit with a corresponding simulated image was employed for thickness determination. This gives a thickness accuracy of approximately $\pm$ 2 nm ($\pm$4 unit cells), limited by the number of simulated patterns calculated. However, the use of PACBED patterns for film thickness evaluation is still an emerging technique and further study is required to fully probe the accuracy and precision limits of this

method. A comparison by eye between the experimental and simulated patterns confirms good agreement by this method. One notable difference, however, is the background contribution derived from thermal diffuse scattering. This effect can be included in the simulation using a frozen phonon model. However, PACBED simulations are particularly computationally demanding, in part because the simulations need to be performed over a large area to produce sufficient resolution in the diffraction plane to distinguish structural detail in the patterns. To save on computing time a simpler absorptive model was used in this case (as is recommend by LeBeau et al.[25]), and the background scatter in the experimental patterns was subtracted from the line scan data for quantitative comparison. Experimental patterns were also scaled and rotated. Published studies to date have employed a combination of by eye comparision and single line scans to evaulate PACBED patterns however, to exploit the full potential of this technique, it would be desirable to develop and validate a computational method to quantitatively evaluate the similarity of experimental and simulated patterns based on pertinent features across the full area of the pattern.
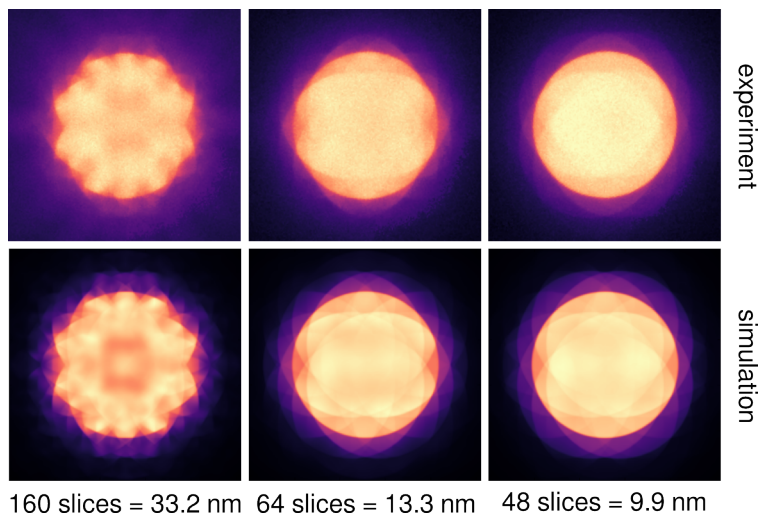

160 slices = 33.2 nm 64 slices = 13.3 nm 48 slices = 9.9 nm

Figure 1: Experimental and corresponding simulated PACBED patterns for three image locations on a single $(InAlAs)_{0.8}(AlAsSb)_{0.2}$ foil.

Quantification of z-contrast images for compositional analysis

Several HAADF images were acquired from the same foil at different locations representing different sample thickness: 33.2 nm, 13.3 nm and 9.9 nm. The z-contrast images shown in Figure 2a are of a low Sb fraction sample: $(InAlAs)_{0.8}(AlAsSb)_{0.2}$. Dumbbell pairs showing cation (In, Al) and anion (As, Sb) atomic columns form a near perfect array in the orientation expected for the $< 110 >$ projection of a zinc blende lattice. All images obtained in this study show a similar level of crystal quality, providing further evidence that the degraded optical properties of this alloy do not derive from structural point or extended defects such as vacancies or dislocations. From careful examination of the z-contrast images, it is observed that the intensity ratios between anion and cation columns vary for different dumbbell sites across each image. However, clustering is not observable from simple visual inspection. Quantification of the z-contrast images is necessary to fully interpret these images.

Quantification process

Different elements present in the alloy have a range of atomic numbers: In (49), Al (13), As (33), Sb (51), and hence chemical information can be extracted from the images based on z-contrast. A quantification process, comparing anion and cation intensity ratios, was applied to the z-contrast images (Figure 2b), similar to the methods described in the literature.[27,28] Dumbbell locations were identified using a peak-finding algorithm which differentiates image intensity in the x and y directions to find local maxima. A line scan was then performed at each peak location and two Gaussian peaks were fit to the intensity data to determine the relative cation and anion column intensities. Peak intensity and background were fitting variables, while the Gaussian width was fixed for each pair. The relative Gaussian intensity (above the background) of anion and cation columns (I_{an}/I_{cat}) was then mapped (Figure 2c) to provide insight into the compositional distribution. A high value is representative of
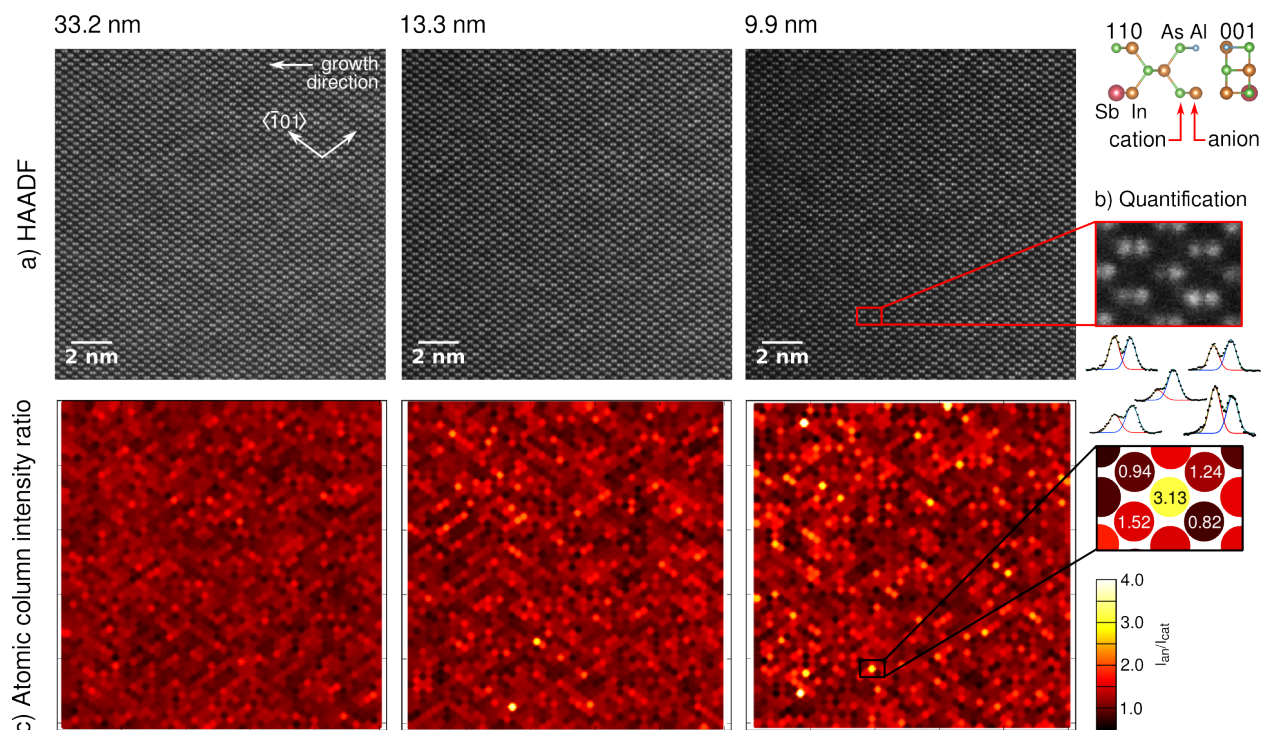
Figure 2: a) HAADF images from a single InAlAsSb foil with thicknesses: 33.2 nm, 13.3 nm and 9.9 nm. No post processing has been applied to the images. An example atomic model is also shown for two atomic layers in the 110 and 001 projections. Full size, as acquired TIA files are provided in supporting material. b) Illustration of the quantification process flow for a small area of the image. A line scan is performed across each dumbbell and two Gaussian peaks are fitted to the scan, one for each atomic column. The ratio of anion and cation column intensities (I_{an}/I_{cat}) relates to the atomic masses present within each column. c) I_{an}/I_{cat} ratio is mapped for each image using interpolation to fill void spaces between the dumbells. From visual inspection, it appears that atomic column pairs with high I_{an}/I_{cat} values (high Sb fraction) typically align in rows along the $< 101 >$ and $< \bar{1}01 >$ crystal axes.

a high mass value in the anion column and hence a large Sb fraction, while a low value is representative of a high mass value in the cation column and hence a large In fraction.

Atomic column intensity ratio maps suggest clustering

The maps shown in Figure 2c highlight the wide variation in atomic column composition across each image, with the greatest variation observed in the thinnest sample. The maps are also suggestive of the formation of clusters in rows along the $< 101 >$ and $< \overline{1}01 >$ crystal axes. That said, a visual interpretation of patterns in the images can easily be misleading, hence a statistical comparison with a simulated random structure is necessary to draw firm conclusions on clustering. Table 1 provides statistical data on I_{an}/I_{cat} for each of the experimental images acquired, along with foil thickness as evaluated by PACBED. While these data are intended primarily for quantitative comparison with the simulation, several trends between the measurements are also noted. As the foil thickness increases, a slight decrease in I_{an}/I_{cat} is observed (8% reduction for a thickness increase of 300%). This may be a result of cross-talk between neighboring columns, whereby the channeling electron beam is briefly displaced to a neighboring column so as to reduce the relative z-contrast between the two columns.[29,30] A substantial reduction in the I_{an}/I_{cat} standard deviation is also observed as the foil thickness increases. Variations may originate from two sources: random variation in the multi-species alloy and short length scale clustering. Both of these effects are reduced in a thicker layer, as the variation is averaged across the foil volume so as to produce a more homogeneous I_{an}/I_{cat} map. It is possible to deconvolve these two effects by calculating the I_{an}/I_{cat} standard deviation occurring in a truly random simulated alloy, and thus determine the contribution from clustering.

Table 1: I_{an}/I_{cat} statistical parameters for an $(InAlAs)_{0.8}(AlAsSb)_{0.2}$ sample with different foil thicknesses. Figure 2 shows the z-contrast images and corresponding I_{an}/I_{cat} intensity maps used to compile the data in this table.

Foil thickness (nm)	Average I_{an}/I_{cat}	Standard deviation I_{an}/I_{cat}
9.9	1.196	0.382
13.3	1.144	0.275
33.2	1.103	0.196

Comparison of experimental and simulated STEM images

To perform the simulation, random alloys of $(InAlAs)_x(AlAsSb)_{1-x}$ were generated. Periodic structures were aligned along the $< 110 >$ crystal axis, with x-y dimensions 1.76 x 1.66 nm and z dimension 53.13 nm. This corresponds to 24 atomic column pairs formed of 256 atomic layers. STEM image simulations were performed on the structures using Dr. Probe multi-slice software. Structures were sampled 384 times in each dimension to calculate phase gratings. Images with 96 x 96 probe positions were then simulated, corresponding to an image pixel resolution of ∼18 pm. Three frozen phonon configurations were considered per pixel, and an a-posteriori Gaussian source convolution was applied for a source size of 0.05 nm (HWHM). The first two layers along the beam direction $(InAlAs)_x(AlAsSb)_{1-x}$ for x = 0.2, 0.8 and 1.0 random alloys are shown in Figure 3a, and the corresponding STEM simulation in Figure 3b. It is observed that the locations of high mass atoms in the lattice correspond to high z-contrast in the image simulation. After only two layers, different atomic column pairs across the simulated image exhibit significant variations in the relative anion and cation intensities. This occurs because of random variation in the quaternary alloy. The STEM simulation for a 64-layer random alloy representing 13.3 nm thickness (Figure 3c) shows that random variation in the STEM image significantly decreases as a function of thickness. For this reason, accurately determining the layer thickness is essential if random variation and short length scale clustering along the beam direction are to be reliably distinguished in this alloy. From Figure 3c, it is observed qualitatively that the structure with high Sb fraction (x=0.2) has the highest I_{an}/I_{cat} intensity ratio.
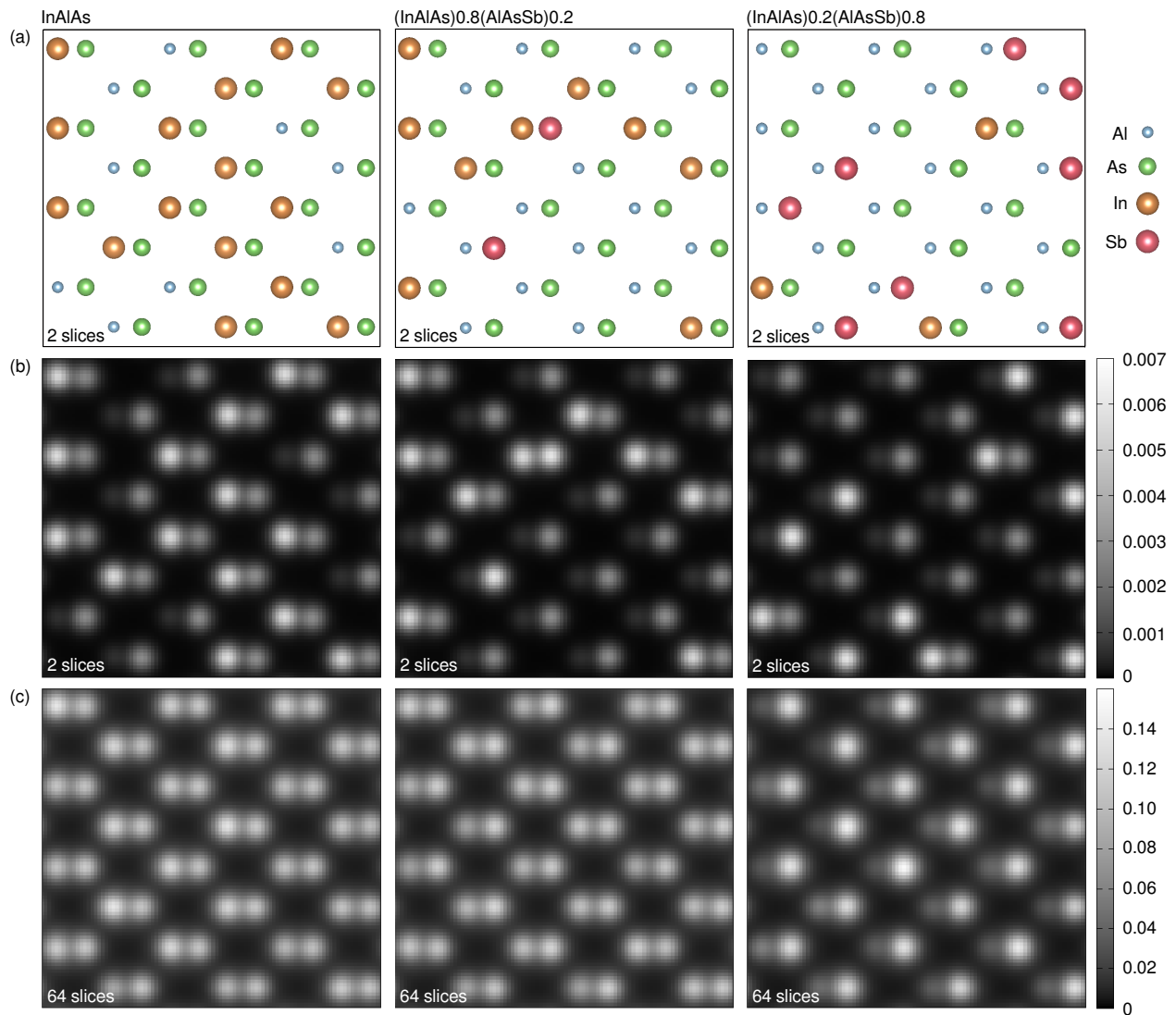
Figure 3: a) First two slices of simulated $(InAlAs)_x(AlAsSb)_{1-x}$ random alloy structures with x = 0.2, 0.8 and 1.0. Visualized using VESTA software.[31] b) Simulated STEM images after the first two slices of the structures. c) Simulated STEM images after the first 64 slices of the structures.

Quantification process applied to simulated images

The quantification process applied to the experimental images, outlined in Section 3, was also used to evaluate I_{an}/I_{cat} from the simulated images. Figure 4 shows the average I_{an}/I_{cat} ratio after 64 slices (13.3 nm) as a function of composition x for random $(InAlAs)_x(AlAsSb)_{1-x}$ alloys, along with the standard deviation for each composition. It is important to note that in this case standard deviation does not relate to measurement uncertainty, but instead derives from the random variation of the quaternary alloy.
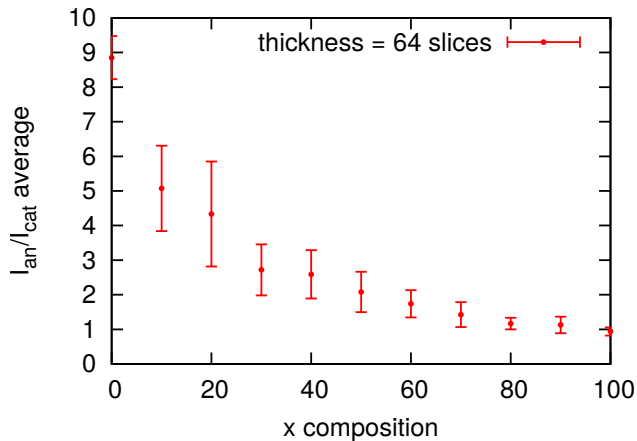

Figure 4: Average I_{an}/I_{cat} ratio evaluated from multi-slice image simulations as a function of x for $(InAlAs)_x(AlAsSb)_{1-x}$ random alloys for 64 slices. Bars show I_{an}/I_{cat} standard deviations.

Atomic column intensity ratio is highly dependent on sample composition and foil thickness

As expected, the simulations for structures with high Sb fraction (low x) yield the highest average I_{an}/I_{cat} ratio. It is not a simple linear relationship, however, indicating that for quaternary alloys quantitative comparison between simulation and experiment requires explicit simulation of the given composition. For example, it is insufficient to simply interpolate between the values derived for the ternary endpoints. The standard deviation also changes for different compositions. The two ternary endpoints exhibit the lowest standard deviations

12

as a percentage, because they have one fewer atomic species whose alloy concentration may vary. Simulated dependences of I_{an}/I_{cat} on thickness are shown in Figure 5 for x = 0.2, 0.8 and 1.0. For all compositions, the variations are found to be significant. $I_{an}/I_{cat} > 1.0$ for both x = 0.2 and 0.8, which gradually decreases with increasing thickness. This behavior is also observed in the experimental images for x = 0.8. However, the reverse trend is observed in the simulations for x = 1.0, which yields $I_{an}/I_{cat} < 1.0$ for thin structures. This inverse behavior provides further evidence that the thickness dependence of I_{an}/I_{cat} results from channeling and cross-talk between neighboring columns, which reduces the z-contrast between atomic column pairs such that I_{an}/I_{cat} tends towards unity as the sample thickness increases. This further highlights the importance of evaluating the sample thickness when quantitatively comparing with simulations. It also suggests that sample tilt will impact the atomic column intensity ratio.

Reducing sample tilt

The simulated structures are positioned perpendicular to the converged beam. However, in the experiment a small tilt may be present, which reduces the contributions from channeling present in the STEM image. This, in turn, will change the degree of cross-talk between neighboring columns and hence the atomic column intensity ratio. PACBED patterns are particularly sensitive to the presence of sample tilt,[25] and thus provide a visual tool for estimating the sample thickness as well as confirming good sample alignment. Both are required for reliable quantitative comparison between experiment and simulation.

Evidence for alloy clustering

Figure 5 also shows I_{an}/I_{cat} values determined from the experimental images (Table 1) for the x = 0.8 composition. While the average experimental I_{an}/I_{cat} values agree well with the simulations, the standard deviations are significantly larger in the experimental case. For example, the value determined experimentally for the 9.9-nm-thick sample is 56% larger
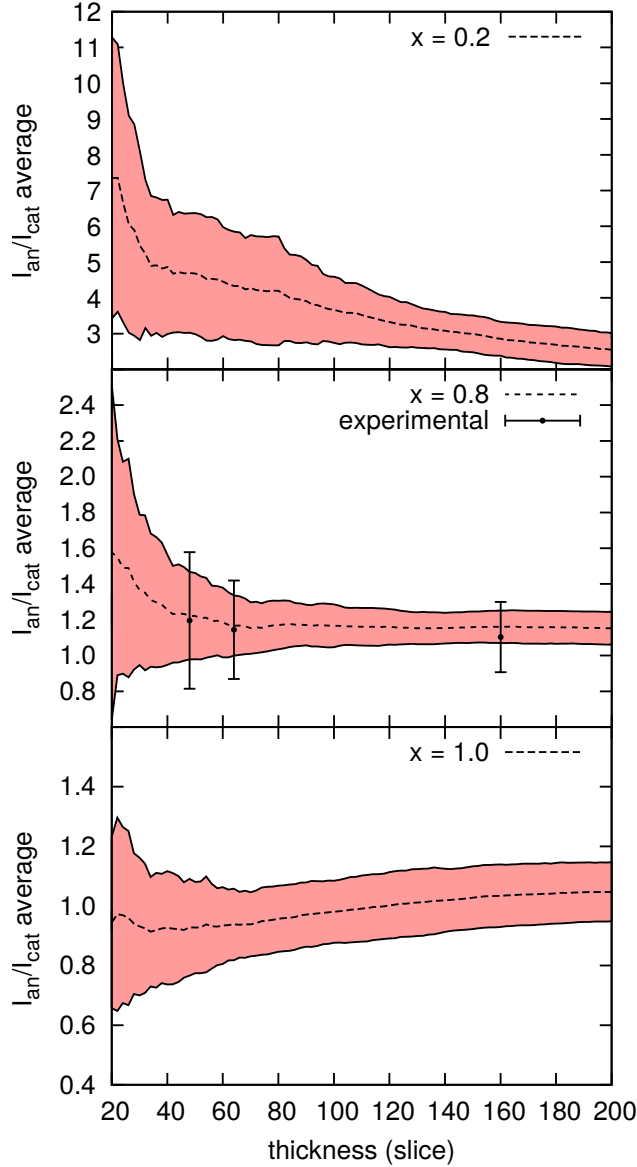
Figure 5: Average I_{an}/I_{cat} ratios evaluated from multi-slice image simulations as a function of thickness for x = 0.2, 0.8, 1.0. Shaded regions show the I_{an}/I_{cat} standard deviation. For x = 0.8, the average I_{an}/I_{cat} values determined from the experimental images are marked along with the experimental standard deviation. The standard deviation of the experimental data exceeds that of the simulation, implying the presence of phase separation in the experimental samples. The thickness range of 20-200 slices is equivalent to ∼4-40 nm

than the corresponding simulated value. Thus the experimental sample exhibits variations in the atomic column ratio over and above those expected solely from the random alloy variations accounted for in the simulations. This additional variation may be attributed to clustering in the alloys grown by MBE, consistent with our visual interpretation of the atomic column contrast maps and previous photoluminescence results on similar samples. It has been reported previously that exposure to the electron beam during imaging can induce clustering in InGaN that was not present in the as-grown material.[16–18] Hence the experimental method can influence the result. To evaluate the possibility that beam-induced clustering affected our results for InAlAsSb, the beam was scanned continuously over a fixed sample area for a 5 minute time period. Images were acquired at periodic intervals during this scan, and atomic column quantification was performed on the images. These measurements determined that the average atomic column intensity ratio and standard deviation were not substantially altered by the extended beam exposure, and hence beam induced clustering cannot account for the observed differences in compositional variation between the simulated and experimental images. Further information about this evaluation is provided in the supporting information.

Conclusion

Quaternary alloys are increasingly used for novel, high performance optoelectronic device development because target bandgaps can be achieved while maintaining lattice matching to standard growth substrates, by adjusting the relative compositions of the constituent elements. In practice, quaternary alloy growth can be problematic because the immiscibility of certain compositions leads to phase segregation within the solid that degrades the material properties. InAlAsSb is a promising candidate material for a high bandgap sub-cell in a multi-junction device that is fully lattice matched to InP. However, recent studies of this alloy identified photoluminescence behavior that appeared characteristic of phase segregation.

15

In this study, we further probed this phase segregation by using electron microscopy to image the clustering at the atomic scale. Ultra-thin sample lamellae were prepared using a specifically adapted process flow that minimized surface damage, and high-resolution HAADF-STEM images were then acquired at several locations on the lamellae. PACBED patterns were also acquired at each location representing different thickness, to assess the local layer thickness and allow comparison with simulated images. The atomic column intensity ratio (I_{an}/I_{cat}) was quantified in the HAADF images by fitting 1D Gaussian curves to linescans across the dumbbell pairs. The corresponding maps reveal variations in the atomic column intensity ratios, with the greatest variations observed in the thinnest layers. Visual interpretation of the maps suggests that rows of column pairs with high Sb composition form elongated clusters along the $< 101 >$ and $< \bar{1}01 >$ crystal axes.

In ultra-thin layers, compositional variations derive from two sources: random variation in the multi-species alloy and atomic clustering. To distinguish between them, a multislice approach was used to simulate STEM images for a truly random alloy of the same composition. It was determined that the atomic column intensity ratio variation was greater in the experimental images than in the simulation. The additional variation beyond that of a truly random structure is attributed to clustering, in agreement with the qualitative visual interpretation of the atomic column intensity ratio maps and with photoluminescence studies performed on similar samples. Quantification of the simulated images also reveals a significant dependence of the atomic column intensity ratio on thickness, which is attributed to cross-talk between neighboring columns. This highlights the importance of foil thickness measurements for quantitative comparison with the simulations. Measurements on ultra-thin foils were enabled in this study by the PACBED technique.[25] More traditional thickness measurement techniques, such as EELS, may not have provided sufficient accuracy on this short length scale to allow a meaningful quantitative comparison.

The next development step for this material will be to image samples with different MBE parameters, including growth temperature and V-III ratio, as well as post growth anneals,

to observe changing trends in the extent of the compositional variations. The process flow employed in this study can also provide a guide for imaging other material systems, in which atomic scale clustering has previously been difficult to conclusively identify.

Experimental

Samples

The samples used in this study were grown on InP wafers by molecular beam epitaxy. The InAlAsSb layers of thickness 1.5 μm were grown on lattice-matched $In_{0.53}Ga_{0.48}As$ and $AlAs_{0.56}Sb_{0.44}$ buffer layers and then capped with $In_{0.52}Ga_{0.48}As$. The growth temperature of the InAlAsSb layer was 395 °C. Lamellae were prepared for imaging using a procedure specifically optimized to produce ultra-thin, clean foils, which was similar to that described by Wessel.[32] An FEI Nova 600 NanoLab DualBeam focused ion beam was used to prepare grid-mounted lamellae on the order of 200 nm thick at the top and 700 nm thick at the bottom. Final thinning of the lamellae was performed in a Fischionne NanoMill at 900 eV, 150 μA for bulk thickness reduction, and at 500 eV, 120 μA to polish the surface and remove any remaining amorphous material produced during the sample preparation.

HAADF imaging

Images were acquired using the National Center for Microsocopy TEAM I instrument, which is a modified FEI Titan 80-300 TEM/STEM.[33] The microscope was operated in scanning mode at 300 kV, with a convergence semiangle of 17 mrad and an inner detector angle of 48 mrad. Images with 1024 x 1024 pixels were acquired with a dwell time of 29 μs per pixel at 5.1 Mx magnification, equating to a pixel dimension of 15.7 pm.

Acknowledgement

Supporting Information Available

The following files are available free of charge.

- 33p3nm_InAlAsSb.ser: As acquired STEM image file

- 13p3nm_InAlAsSb.ser: As acquired STEM image file

- 9p9nm_InAlAsSb.ser: As acquired STEM image file

- Supporting_information.pdf: Debey-Waller factors used for simulation and a study of beam induced damage

References

1. Adachi, S. Physical properties of III-V semiconductor compounds: InP. *InAs, GaAs* **1992**,

2. Nahory, R.; Pollack, M.; Johnston Jr, W.; Barns, R. Band gap versus composition and demonstration of Vegard's law for $In_{1-x}Ga_xAs_yP_{1-y}$ lattice matched to InP. *Applied Physics Letters* **1978**, *33*, 659–661.

3. Olego, D.; Chang, T.; Silberg, E.; Caridi, E.; Pinczuk, A. Compositional dependence of band-gap energy and conduction-band effective mass of $In_{1-x-y}Ga_xAl_yAs$ lattice matched to InP. *Applied Physics Letters* **1982**, *41*, 476–478.

4. Kopf, R.; Wei, H.; Perley, A.; Livescu, G. Electron effective mass and band-gap dependence on alloy composition of $Al_yGa_xIn_{1-y-x}As$, lattice matched to InP. *Applied physics letters* **1992**, *60*, 2386–2388.

5. Fan, J.; Chen, Y. Effect of disorder-induced band mixing on the conduction-band effective mass of InAlGaAs alloys lattice matched to InP. *Journal of applied physics* **1996**, *80*, 1239–1241.

6. Vurgaftman, I.; Meyer, J.; Ram-Mohan, L. Band parameters for III-V compound semiconductors and their alloys. *Journal of applied physics* **2001**, *89*, 5815–5875.

7. González, M.; Chan, N.; Ekins-Daukes, N. J.; Adams, J. G. J.; Stavrinou, P.; Vurgaftman, I.; Meyer, J. R.; Abell, J.; Walters, R. J.; Cress, C. D. *et al.* Modeling and analysis of multijunction solar cells. Proc. SPIE 7933. 2011; p 79330R.

8. Walters, R. J.; González, M.; Tischler, J. G.; Lumb, M. P.; Meyer, J. R.; Vurgaftman, I.; Abell, J.; Yakes, M. K.; Ekins-Daukes, N. J.; Adams, J. G. J. *et al.* Design of an achievable, all lattice-matched multijunction solar cell using InGaAlAsSb. Photovoltaic Specialists Conference (PVSC), 2011 37th IEEE. 2011; pp 000122–000126.

9. Lumb, M. P.; Gonzalez, M.; Vurgaftman, I.; Meyer, J. R.; Abell, J.; Yakes, M.; Hoheisel, R.; Tischler, J. G.; Jenkins, P. P.; Stavrinou, P. N. *et al.* Simulation of novel InAlAsSb solar cells. SPIE OPTO. 2012; pp 82560S–82560S.

10. González, M.; Lumb, M. P.; Yakes, M. K.; Abell, J.; Tischler, J. G.; Bailey, C. G.; Vurgaftman, I.; Meyer, J. R.; Hirst, L. C.; Schmieder, K. J. *et al.* Modeling, design and experimental results for high efficiency multi-junction solar cells lattice matched to InP. SPIE OPTO. 2014; pp 898117–898117.

11. Hirst, L. C.; Lumb, M. P.; Abell, J.; Ellis, C. T.; Tischler, J. G.; Vurgaftman, I.; Meyer, J. R.; Walters, R. J.; González, M. Spatially indirect radiative recombination in InAlAsSb grown lattice-matched to InP by molecular beam epitaxy. *Journal of Applied Physics* **2015**, *117*, 215704.

12. Cho, Y.-H.; Gainer, G.; Fischer, A.; Song, J.; Keller, S.; Mishra, U.; DenBaars, S. "S-shape" temperature-dependent emission shift and carrier dynamics in InGaN/GaN multiple quantum wells. *Applied Physics Letters* **1998**, *73*, 1370–1372.

13. Baladés, N.; Herrera, M.; Sales, D. L.; Delgado, F.; Hernández-Maldonado, D.; Ramasse, Q.; Pizarro, J.; Galindo, P.; González, M.; Abell, J. *et al.* Structural characterization of InAlAsSb/InGaAs/InP heterostructures for solar cells. *Applied Surface Science* **2016**,

14. Gerthsen, D.; Hahn, E.; Neubauer, B.; Rosenauer, A.; Schön, O.; Heuken, M.; Rizzi, A. Composition fluctuations in InGaN analyzed by transmission electron microscopy. *physica status solidi (a)* **2000**, *177*, 145–155.

15. Bartel, T.; Specht, P.; Ho, J.; Kisielowski, C. Phase separation in $In_xGa_{1-x}N$. *Philosophical Magazine* **2007**, *87*, 1983–1998.

16. Smeeton, T.; Kappers, M.; Barnard, J.; Vickers, M.; Humphreys, C. Electron-beam-induced strain within InGaN quantum wells: False indium "cluster" detection in the transmission electron microscope. *Applied Physics Letters* **2003**, *83*, 5419–5421.

17. Li, T.; Hahn, E.; Gerthsen, D.; Rosenauer, A.; Strittmatter, A.; Reissmann, L.; Bimberg, D. Indium redistribution in an InGaN quantum well induced by electron-beam irradiation in a transmission electron microscope. *Applied Physics Letters* **2005**, *86*, 241911.

18. Galtrey, M. J.; Oliver, R. A.; Kappers, M. J.; Humphreys, C. J.; Stokes, D. J.; Clifton, P. H.; Cerezo, A. Three-dimensional atom probe studies of an $In_xGa_{1-x}N/GaN$

multiple quantum well structure: Assessment of possible indium clustering. *Applied physics letters* **2007**, *90*, 1903.

19. Baloch, K. H.; Johnston-Peck, A. C.; Kisslinger, K.; Stach, E. A.; Gradečak, S. Revisiting the "In-clustering" question in InGaN through the use of aberration-corrected electron microscopy below the knock-on threshold. *Applied Physics Letters* **2013**, *102*, 191910.

20. Kisielowski, C.; Bartel, T. Comment on "Three-dimensional atom probe studies of an InxGa1-xN/GaN multiple quantum well structure: Assessment of possible indium clusterin" Appl. Phys. Lett., 061903 (2007). *Applied Physics Letters* **2007**, *91*, 176101–176101.

21. Tang, F.; Zhu, T.; Oehler, F.; Fu, W. Y.; Griffiths, J. T.; Massabuau, F. C.-P.; Kappers, M. J.; Martin, T. L.; Bagot, P. A.; Moody, M. P. *et al.* Indium clustering in a-plane InGaN quantum wells as evidenced by atom probe tomography. *Applied Physics Letters* **2015**, *106*, 072104.

22. Hernández-Saz, J.; Herrera, M.; Delgado, F.; Duguay, S.; Philippe, T.; Gonzalez, M.; Abell, J.; Walters, R.; Molina, S. Atom-scale compositional distribution in InAlAsSb-based triple junction solar cells by atom probe tomography. *Nanotechnology* **2016**, *27*, 305402.

23. Kotulak, N. A.; Knipling, K. E.; González, M.; Hirst, L. C.; Tomasulo, S.; Abell, J.; Yakes, M. K.; Vurgaftman, I.; Meyer, J. R.; Walters, R. J. Three-dimensional Composition Reconstruction of InAlAsSb Lattice-Matched to InP for Top Cell Implementation. Photovoltaic Specialists Conference (PVSC), 2016 43rd IEEE. 2016; pp In–press.

24. González, M.; Lumb, M. P.; Hirst, L. C.; Tomasulo, S.; Tischler, J. G.; Yoon, W.; Abell, J.; Vurgaftman, I.; Bennett, M. F.; Schmieder, K. J. *et al.* Rapid thermal annealing of InAlAsSb lattice-matched to InP for top cell applications. Photovoltaic Specialist Conference (PVSC), 2015 IEEE 42nd. 2015; pp 1–4.

25. LeBeau, J. M.; Findlay, S. D.; Allen, L. J.; Stemmer, S. Position averaged convergent beam electron diffraction: Theory and applications. *Ultramicroscopy* **2010**, *110*, 118–125.

26. Barthel, J. Dr. Probe-STEM simulation software. `http://www.er-c.org/barthel/drprobe/`, Accessed: October 2015.

27. Robb, P. D.; Craven, A. J. Column ratio mapping: A processing technique for atomic resolution high-angle annular dark-field (HAADF) images. *Ultramicroscopy* **2008**, *109*, 61–69.

28. Sales, D.; Guerrero, E.; Rodrigo, J.; Galindo, P.; Yáñez, A.; Shafi, M.; Khatab, A.; Mari, R.; Henini, M.; Novikov, S. *et al.* Distribution of bismuth atoms in epitaxial GaAsBi. *Applied Physics Letters* **2011**, *98*, 101902.

29. Allen, L.; Findlay, S.; Oxley, M.; Rossouw, C. Lattice-resolution contrast from a focused coherent electron probe. Part I. *Ultramicroscopy* **2003**, *96*, 47 – 63.

30. Kimoto, K.; Asaka, T.; Nagai, T.; Saito, M.; Matsui, Y.; Ishizuka, K. Element-selective imaging of atomic columns in a crystal using STEM and EELS. *Nature* **2007**, *450*, 702–704.

31. Momma, K.; Izumi, F. VESTA 3 for three-dimensional visualization of crystal, volumetric and morphology data. *Journal of Applied Crystallography* **2011**, *44*, 1272–1276.

32. Wessel, A. M. Imaging gallium nitride high electron mobility transistors to identify point defects. Ph.D. thesis, Monterey, California: Naval Postgraduate School, 2014.

33. Ercius, P.; Boese, M.; Duden, T.; Dahmen, U. Operation of TEAM I in a User Environment at NCEM. *Microscopy and Microanalysis* **2012**, *18*, 676–683.

Graphical TOC Entry